



Distant Comet C/2017 K2 and the Cohesion Bottleneck

David Jewitt^{1,2}, Jessica Agarwal³, Man-To Hui¹, Jing Li¹, Max Mutchler⁴, and Harold Weaver⁵¹ Department of Earth, Planetary and Space Sciences, UCLA, 595 Charles Young Drive East, Los Angeles, CA 90095-1567, USA; jewitt@ucla.edu
² Department of Physics and Astronomy, University of California at Los Angeles, 430 Portola Plaza, Box 951547, Los Angeles, CA 90095-1547, USA
³ Max Planck Institute for Solar System Research, Justus-von-Liebig-Weg 3, D-37077 Göttingen, Germany⁴ Space Telescope Science Institute, 3700 San Martin Drive, Baltimore, MD 21218, USA⁵ The Johns Hopkins University Applied Physics Laboratory, 11100 Johns Hopkins Road, Laurel, MD 20723, USA

Received 2018 October 5; revised 2018 November 14; accepted 2018 November 20; published 2019 January 23

Abstract

The distant long-period comet C/2017 K2 (PANSTARRS) has been outside the planetary region of the solar system for ~ 3 Myr, negating the possibility that heat retained from the previous perihelion could be responsible for its activity. This inbound comet is also too cold for water ice to sublimate and too cold for amorphous water ice, if present, to crystallize. C/2017 K2 thus presents an ideal target in which to investigate the mechanisms responsible for activity in distant comets. We have used the *Hubble Space Telescope* to study the comet in the pre-perihelion heliocentric distance range $13.8 \leq r_H \leq 15.9$ au. In this range, the coma maintains a logarithmic surface brightness gradient $m = -1.010 \pm 0.004$, consistent with mass loss proceeding in steady state. The absence of a radiation pressure swept tail indicates that the effective particle size is large (radius $\gtrsim 0.1$ mm) and the mass-loss rate is $\sim 200 \text{ kg s}^{-1}$, remarkable for a comet still beyond the orbit of Saturn. Extrapolation of the photometry indicates that activity began in 2012.1 ± 0.5 , at $r_H = 25.9 \pm 0.9$ au, where the isothermal blackbody temperature is only $T_{BB} = 55$ K. This large distance and low temperature suggest that cometary activity is driven by the sublimation of a super-volatile ice (e.g., CO), presumably preserved by K2's long-term residence in the Oort cloud. The mass-loss rate can be sustained by CO sublimation from an area $\lesssim 2 \text{ km}^2$, if located near the hot subsolar point on the nucleus. However, while the drag force from sublimated CO is sufficient to lift millimeter-sized particles against the gravity of the cometary nucleus, it is 10^2 – 10^3 times too small to eject these particles against interparticle cohesion. Our observations thus require either a new understanding of the physics of interparticle cohesion or the introduction of another mechanism to drive distant cometary mass loss. We suggest thermal fracture and electrostatic supercharging in this context.

Key words: comets: general – comets: individual (C/2017 K2) – Oort Cloud

1. Introduction

The sublimation of water ice can drive cometary activity out to about the orbit of Jupiter (5 au), as proposed in the original “dirty snowball” model of the nucleus by Whipple (1950). However, some comets, of which the long-period comet C/2017 K2 (PANSTARRS; hereafter “K2”) is a prime example, show activity at much larger distances. Comet K2 was active at discovery (heliocentric distance $r_H = 15.9$ au) and was later found to be active in prediscovery data out to $r_H = 23.7$ au (Jewitt et al. 2017b; Meech et al. 2017; Hui et al. 2018). Significantly, K2 is on a long-period orbit and approaching perihelion, which removes the possibility that the observed mass loss is driven by the activation of subsurface volatiles by conducted heat acquired near perihelion. Comet K2 is entering the planetary region of the solar system from Oort cloud distances and temperatures, retaining negligible heat from the previous perihelion.

The osculating orbit of K2 is marginally hyperbolic (semimajor axis $a = -5034$ au, perihelion distance $q = 1.810$ au, eccentricity $e = 1.00036$, and inclination $i = 87.5^\circ$) with perihelion expected on UT 2022 December 21. The slight excess eccentricity above unity is a product of planetary perturbations, as shown by numerical integrations that reveal a pre-entry semimajor axis $a \sim 20,000$ au, eccentricity $e = 0.9998$, and orbit period ~ 3 Myr (Królikowska & Dybczyński 2018). K2 is thus not dynamically new in the Oort sense, but is a return visitor to the planetary region. Crucially, however, with the previous perihelion occurring

~ 3 Myr ago, it is clear that current activity in K2 cannot be related to heat retained from the previous approach.

The scientific excitement of K2 is that it provides an opportunity to study the rise of cometary activity in a never-before-observed distance regime. *Hubble Space Telescope* (*HST*) observations of K2 from a single orbit were reported in Jewitt et al. (2017b). In this paper, we describe continuing observations with *HST*, taken to study the early development of the coma as K2 approaches the Sun. During our observations the comet approached from $r_H = 15.9$ to 13.8 au. Our *HST* data have the advantages of high angular resolution and of being taken with a single observational system.

2. Observations

For the present observations we used images from the WFC3 imaging camera on the 2.4 m *HST*, taken under observational programs GO 15409 and 15423. The UVIS channel of this instrument uses two thinned, backside-illuminated charge-coupled devices (CCDs) each with 2051×4096 pixels, separated by a 35 pixel gap. The image scale is $0''.04 \text{ pixel}^{-1}$ across a field $162'' \times 162''$. To reduce overhead times, we read out only a smaller CCD subarray, giving an $81'' \times 81''$ field of view. We used the wide F350LP filter in order to maximize sensitivity to faint sources in the data. This filter benefits from a peak system throughput of 29% and takes in most of the optical spectrum with wavelengths $\lambda > 3500 \text{ \AA}$. The effective wavelength on a Sun-like spectrum source is 5846 \AA and the effective full width at half maximum is 4758 \AA . A journal of

Table 1
Observing Geometry

UT Date and Time	DOY ^a	r_H ^b	Δ ^c	α ^d	$\theta_{-\odot}$ ^e	θ_{-V} ^f	δ_{\oplus} ^g
2017 Jun 28 20:09–20:52 ^h	179	15.869	15.811	3.67	166.3	357.2	0.59
2017 Nov 28 17:08–17:52	332	14.979	15.133	3.71	17.1	358.3	1.38
2017 Dec 18 22:30–23:13	352	14.859	15.010	3.73	358.4	357.3	0.08
2018 Mar 17 09:28–10:34	441	14.331	14.328	3.98	275.6	353.3	−3.97
2018 Jun 15 15:40–16:19	531	13.784	13.668	4.21	181.3	356.3	−0.28

Notes.

^a Day of Year, DOY = 1 on UT 2017 January 01.

^b Heliocentric distance, in astronomical units.

^c Geocentric distance, in astronomical units.

^d Phase angle, in degrees.

^e Position angle of projected anti-solar direction, in degrees.

^f Position angle of negative projected orbit vector, in degrees.

^g Angle from orbital plane, in degrees.

^h Observations from GO 14939, described in Jewitt et al. (2017b).

observations is given in Table 1, where dates are expressed as Day of Year (DOY) with DOY = 1 on UT 2017 January 01.

In each *HST* orbit, we obtained six integrations of 285 s each (1710 s per orbit). The individual images from *HST* are strongly affected by cosmic rays. A cosmetically clean image was obtained by computing the median of the six images from each orbit after first shifting them to a common center. The median images were also rotated to the correct orientation (north up and east left) prior to measurement (Figure 1). The coma is distinguished by its largely circular isophotes, especially inside projected angles $\theta \leq 5''$, and by the absence of any clear change in the morphology as the Earth moved from one side of the orbital plane to the other (plane-crossing corresponds to the UT 2017 December 18 panel in Figure 1).

2.1. Surface Brightness Profile

We computed the surface brightness profile, $\Sigma(\theta)$, as a function of the angular distance, θ , measured from the photocenter of the comet. For this purpose we used a set of 100 annular digital apertures, each 4 pixels ($0''.16$) wide and extending to 400 pixels ($16''$) radius. We determined the sky background in an adjacent annulus extending from 400 to 500 pixels ($16''$ – $20''$). The limitation to the surface brightness measurements is largely set by the accuracy of sky background subtraction. In *HST* data the background appears faintly structured, above photon and detector noise, owing to field stars and galaxies trailed across the images by the nonsidereal tracking of the telescope that is required to keep K2 fixed (see Figure 1). These trails are suppressed by computation of the orbital median image but typically cannot be entirely removed. As a result, the sky uncertainty is non-Gaussian and varies from image to image and orbit to orbit, depending on the background field. We used image statistics within the sky annulus and inspection of line plots through the sky regions in order to estimate the sky uncertainty.

The main result is that the profile of K2 did not change in the 2017–2018 period. In Figure 2 we show profiles from the first (UT 2017 June 28; green symbols) and last (UT 2018 June 15; yellow symbols) observations, together with their uncertainties. In the central region $\Sigma(\leq 0''.2)$ is affected by convolution of the intrinsic cometary profile with the point-spread function of *HST*. In the outer region, $\theta \gtrsim 2''$, the effects of sky subtraction uncertainty become significant. In the $0''.2 \leq \theta \leq 2''.0$ range,

the surface brightness is well-fitted by a power law, $\Sigma(\theta) \propto \theta^m$, with $m = -1.008 \pm 0.004$ on UT 2017 June 28 and $m = -1.012 \pm 0.004$ on UT 2018 June 15. Within the uncertainties, these values are equivalent and the mean, $m = -1.010 \pm 0.004$, is very close to the $m = -1$ slope expected of a coma produced in steady state (Jewitt & Meech 1987). Although the measurement on UT 2018 June 15 is formally different from $m = -1$ at the 3σ confidence level, we prefer to interpret the fits as setting a 3σ limit to the gradient of $m > -1.012$.

The surface brightness profiles of K2 are remarkable for their stability, and for their closeness to the $m = -1$ profile expected of a steady-state coma in the absence of radiation pressure. Radiation pressure acceleration of dust particles should, in the limiting case, produce a tail and steepen the gradient measured within concentric circular apertures to $m = -3/2$ (Jewitt & Meech 1987), very different from the measured gradient. The faintest isophotes in Figure 1 do show asymmetry toward the northwest that, if real, might be caused by solar radiation pressure, but deeper observations and better background removal are needed to establish the reality of the faint, outer regions.

2.2. Aperture Photometry

On a diffuse source, the choice of photometry aperture is critical to the quantitative interpretation of the data. We scaled the photometry apertures inversely with the instantaneous geocentric distance, Δ , so as to maintain fixed linear radii of 5, 10, 20, 40, 80, and 160×10^3 km when projected to the distance of the comet. The smallest of these apertures corresponds to an angular radius $\sim 0''.4$ at geocentric distance $\Delta = 15$ au. This is $\sim 5\times$ the full width at half maximum of the point-spread function, sufficient to avoid complications in the interpretation of the photometry caused by the finite resolution of the data. The background sky brightness and its uncertainty were estimated from the median and dispersion of data numbers in a concentric annulus with inner and outer radii of 400 and 500 pixels ($16''$ and $20''$), respectively. The photometry was calibrated assuming that a G2V source with $V = 0$ would give a count rate $4.72 \times 10^{10} \text{ s}^{-1}$ in the same filter. In the interest of uniformity, we also reanalyzed the images from the preceding program GO 14939 (see Jewitt et al. 2017b) using exactly the same procedures as those applied to the new data.

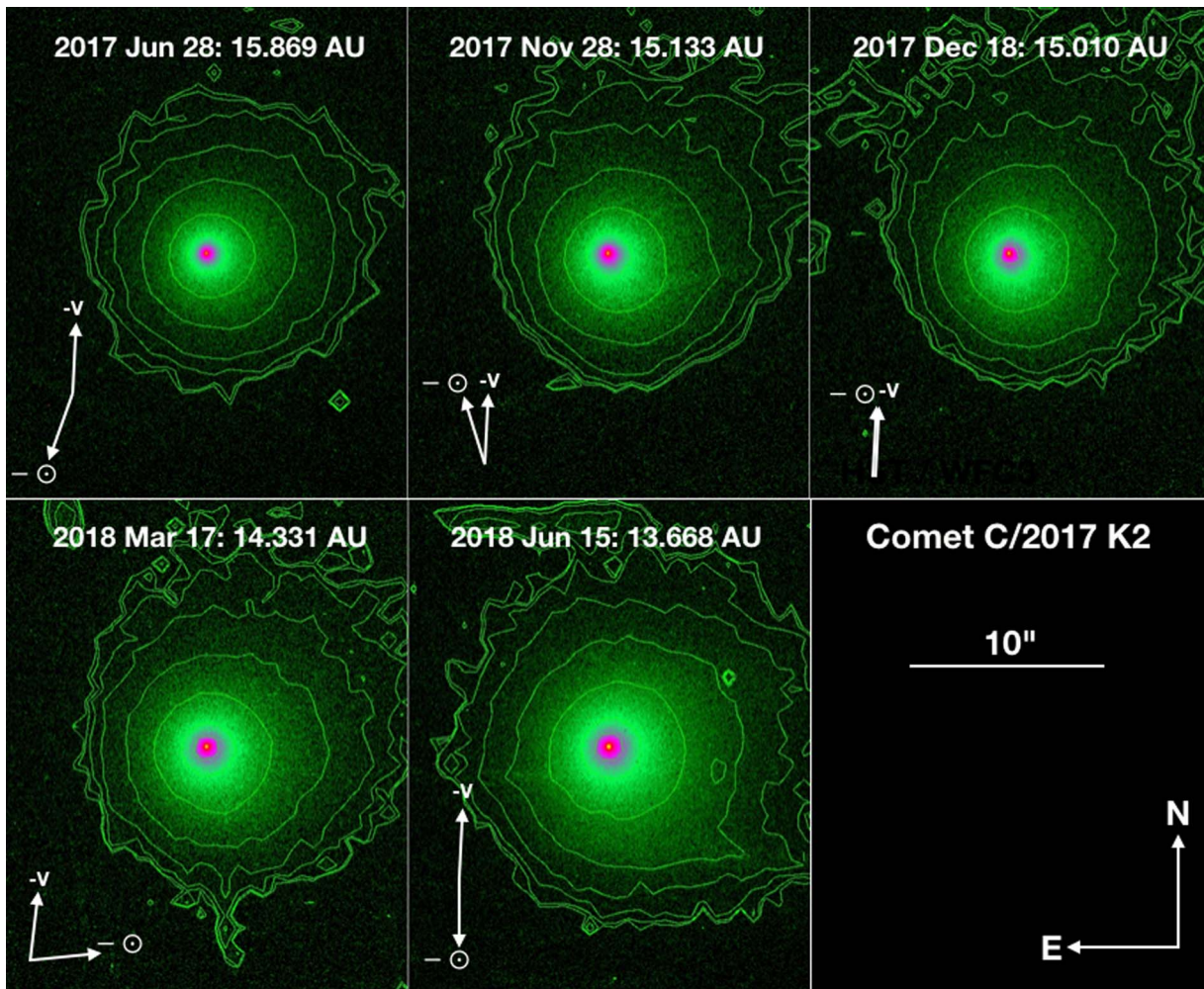


Figure 1. Hubble images of C/2017 K2 marked with their UT dates (see Table 1). White arrows show the projected negative heliocentric velocity vector, marked - v , and the anti-solar direction, marked $-\odot$, respectively. Linear features (e.g., 2018 March 17 and June 15 panels) are the imperfectly removed trails of field stars and galaxies. A scale bar and the cardinal directions are marked in the lower right.

Results from the reanalysis are consistent with those reported earlier, giving confidence that no systematic effects exist between the two data sets.

The photometric measurements are listed in Table 2 where, in addition to the apparent magnitudes, the table lists the absolute magnitudes, H , and the effective scattering cross-sections of the comet, C_e , computed as follows. The absolute magnitude, H , is the magnitude that would be observed if the comet could be relocated to unit heliocentric and geocentric distances, $r_H = \Delta = 1$ au, and to phase angle $\alpha = 0^\circ$. We computed H from the inverse square law, expressed as

$$H = V - 5 \log_{10}(r_h \Delta) - f(\alpha), \quad (1)$$

where V is the apparent magnitude and $f(\alpha)$ is the phase function. The phase functions of comet dust are in general poorly known and, in K2, the phase function is unmeasured. However, K2 was observed at very small and barely changing phase angles (Table 1) so that phase corrections are not a significant source of error. We used $f(\alpha) = 0.04\alpha$, but values half or twice as large would introduce insignificant relative errors in the derived H magnitudes.

The absolute magnitude is related to the effective scattering cross-section, C_e [km^2], by

$$C_e = \frac{1.5 \times 10^6}{p_V} 10^{-0.4H}, \quad (2)$$

where p_V is the geometric albedo. We assume $p_V = 0.04$, consistent with the low albedos measured for the surfaces of cometary nuclei. The apparent and absolute magnitudes and the scattering cross-sections are listed in Table 2 for each aperture and date of observation using the compact format $V/H/C_e$.

3. Discussion

3.1. Initiation of the Activity

3.1.1.

The cumulative effective scattering cross-section, C_e , is plotted as a function of the time of observation in Figure 3, for circular apertures of increasing radius. All the apertures show a steady brightening of the comet with time which, because we have corrected for geometric effects, must reflect changes in the level of activity of the comet. Specifically, the brightening

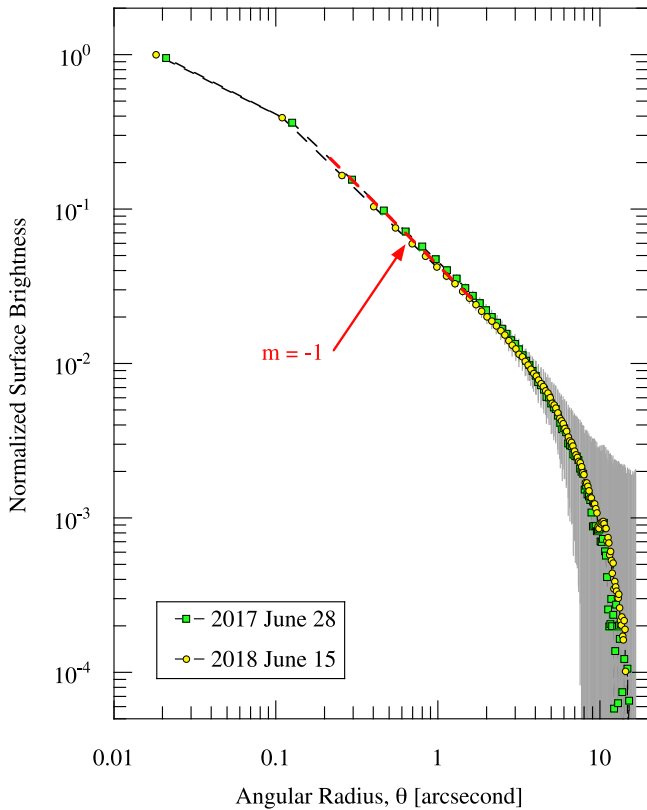


Figure 2. Comparison of surface brightness profiles measured in 2017 June (green squares) and 2018 June (yellow circles). Profile uncertainties resulting from the sky background are shown by the shaded gray region. The red line shows a logarithmic gradient $m = -1$, expected of steady-state coma production.

reflects the difference between the addition of new material from the nucleus and the loss of older material from the edges of the photometry aperture owing to outward expansion of the coma. We computed differential cross-sections, ΔC_e , to measure the amount of dust within each aperture from Table 2 and show them as a function of time in Figure 4. Straight lines in the figure show linear least-squares fits of the form $\Delta C_e = f + gt$, where t is the epoch of observation and f and g are constants for each annulus. Best-fit values of f and g are given in Table 3, along with the initiation time (i.e., the time when $\Delta C_e = 0$) computed from $t_0 = -f/g$. The latter is expressed both as the number of days prior to UT 2017 January 01 and as decimal year and we further list the heliocentric distance at the initiation time. As expected from Figures 3 and 4, uncertainties in the best-fit values of f and g , and so of t_0 , grow with aperture radius because of the effects of noise on the low surface brightness outer coma. The annular cross-sections, ΔC_e , and the calculated initiation times, t_0 , are independent. The weighted mean initiation time is $t_0 = -1772 \pm 171$ DOY, corresponding to year 2012.1 ± 0.5 , at which time the heliocentric distance of K2 was $r_H = 25.9 \pm 0.9$ au (see Figure 5). Clearly, t_0 is approximate, since we have assumed without proof that the rate of brightening measured in the period 2017–2018 held constant at earlier times. However, we note that our estimated value of t_0 precedes the first archival observations that showed K2 to be active in 2013 May (Jewitt et al. 2017b), by about a year. We conclude that the data are consistent with activity beginning $\tau \sim 6.3 \pm 0.4$ yr ($\sim 2 \times 10^8$ s) before the most recent observations (Table 1), when the comet was inbound and ~ 26 au from the Sun.

We separately fitted the heliocentric variation of the cross-section, represented by a power law of the form $\Delta C_e \propto r_H^\gamma$ finding $\gamma = -1.5 \pm 0.6$ from a fit to the $\ell = 160,000$ km aperture photometry (Table 2). The large uncertainty reflects the small fractional change in heliocentric distance over the period of observations. Within 1σ , the data are consistent with a production function that varies with the inverse square of r_H .

Distant pre-perihelion dust ejection has been inferred in some other comets from the position angles and lengths of their tails. For example, Sekanina (1973, 1975) inferred that dust was ejected from long-period comet C/1954 O2 (formerly 1955 VI (Baade)) starting 500–1500 days before perihelion, at heliocentric distances $r_H = 6$ to 12 au. Comet C/Bowell (1980b) likewise showed evidence for early (11 or 12 au), low speed ejection (Sekanina 1982). Comet C/2010 U3 (Boattini) was discovered at $r_H = 18.3$ au inbound, implying coma production at even greater distances. C/2013 A1 (Siding Spring) ejected $100 \mu\text{m}$ particles when beyond Jupiter (Ye & Hui 2014). Even by the standards of these unusual comets, though, the distant activity in K2 must be regarded as extreme.

3.2. Particle Size and Speed

A firm lower limit to the dust speed, U , can be set by the requirement that dust ejected in 2012 should reach or pass the edge of the $160,000$ km radius aperture by 2018. This limit is $U > 0.8 \text{ m s}^{-1}$.

A better estimate of the speed can be obtained by considering the motions of the ejected particles under the action of external forces. The distance over which radiation pressure can accelerate a particle in time, t , is simply

$$L = \frac{\beta g_\odot t^2}{2r_H^2}, \quad (3)$$

where $g_\odot(1) = 0.006 \text{ m s}^{-2}$ is the solar gravity at $r_H = 1$ au and r_H is expressed in astronomical units. The radiation pressure acceleration factor, β , depends on particle composition and shape but, most importantly, on the particle radius. To a useful level of approximation for dielectric spheres, we write $\beta = 1/a_{\mu\text{m}}$, where $a_{\mu\text{m}}$ is the radius expressed in microns. A $1 \mu\text{m}$ sized particle has $\beta \sim 1$. For example, $1 \mu\text{m}$ particles at $r_H = 14$ au would travel $L \sim 5 \times 10^{11}$ m (3 au) in the 6 yr since 2012, producing a tail of angular scale $L/\Delta \sim 14^\circ$ viewed from the distance of K2. Even given that the angular extent of such a tail would be reduced by a projection factor $\tan(\alpha = 4^\circ) \sim 0.07$, its absence in Figure 1 immediately shows that the particles must be large, with $\beta \ll 1$ ($a_{\mu\text{m}} \gg 1$), as previously noted (Jewitt et al. 2017b). In fact, if we accept that no tail is evident on angular scales $\theta \sim 10''$ (Figure 1), then Equation (3) gives $\beta < 0.003$ ($a_{\mu\text{m}} > 350$), implying the dominance of millimeter-sized particles.

We simulated the appearance of K2 using a Monte Carlo model to better assess the size of the particles. In the model, dust particles with a range of sizes are ejected from the Sun-facing hemisphere, with activity beginning in 2012.1 as indicated by the data. The particle sizes occupy a differential power-law distribution with index -3.5 and the ejection velocity, U , is scaled according to $U = U_1 a^{-1/2}$, where U_1 is the velocity of a particle having radius $a = 1$ mm. The inverse square-root relation is expected if gas drag is responsible. The models were computed for the observation on UT 2018 June 15 because, on this date, the anti-solar and projected orbit directions

Table 2
HST Fixed-aperture Photometry^a

UT Date	$\ell/10^3 = 5$	10	20	40	80	160
2017 Jun 28	21.59/9.45/6.22	20.80/8.66/12.9	20.04/7.90/25.9	19.34/7.20/49.4	18.83/6.69/79.1	18.63/6.49/95.1
2017 Nov 28	21.31/9.38/6.64	20.54/8.61/13.5	19.78/7.85/27.2	19.09/7.16/51.3	18.64/6.71/77.6	...
2017 Dec 18	21.31/9.42/6.40	20.52/8.63/13.2	19.74/7.85/27.2	19.03/7.14/52.2	18.53/6.64/82.8	18.27/6.38/105.2
2018 Mar 17	21.03/9.31/7.08	20.26/8.54/14.4	19.49/7.77/29.2	18.80/7.08/55.2	18.32/6.60/85.9	18.13/6.41/102.9
2018 Jun 15	20.81/9.27/7.34	20.05/8.51/14.8	19.29/7.75/29.8	18.57/7.03/57.8	18.02/6.48/95.9	17.78/6.24/119.0

Note.

^a For each date and aperture radius, ℓ (measured in units of 10^3 km at the comet), the table lists the apparent magnitude, V , the absolute magnitude, H , and the scattering cross-section, C_e (in units of 10^3 km²), in the order VH/C_e . C_e is computed from H using Equation (2).

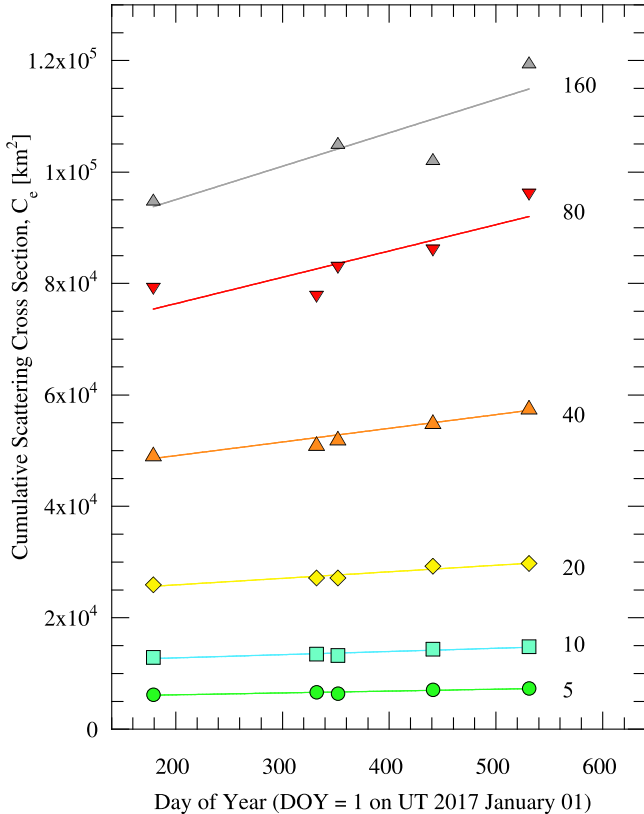


Figure 3. Scattering cross-section as a function of the date of observation for each of six photometry apertures. The radii of the apertures, expressed in units of 10^3 km, are indicated on the plot. Lines are added to guide the eye.

are particularly widely separated, clearly exposing the competitive effects of radiation pressure and solar gravity. We present four examples in Figure 6, for particle radii $1 \leq a \leq 10 \mu\text{m}$, $10 \leq a \leq 100 \mu\text{m}$, $100 \leq a \leq 1000 \mu\text{m}$, and $1 \leq a \leq 10 \text{mm}$ to show the effects of particle size. The $1 \leq a \leq 10 \mu\text{m}$ and $10 \leq a \leq 100 \mu\text{m}$ particles are highly responsive to radiation pressure, adopting the familiar umbrella-shaped distribution with the tail pointed toward the anti-solar direction. Larger particles, with $100 \leq a \leq 1000 \mu\text{m}$ and $1 \leq a \leq 10 \text{mm}$, show a much more nearly isotropic distribution like that in K2 and show, instead, a hint of a (large particle) tail in the direction of the projected orbit. The simulations confirm that the circular isophotes of K2 reflect particles so large as to be insensitive to solar radiation pressure. We adopt a nominal minimum particle radius $a = 0.1 \text{mm}$, and we find that $U_1 = 4 \text{m s}^{-1}$ (consistent with the lower limit identified above) best represents the scale of the coma in our data. At this speed, a 1 mm particle would take

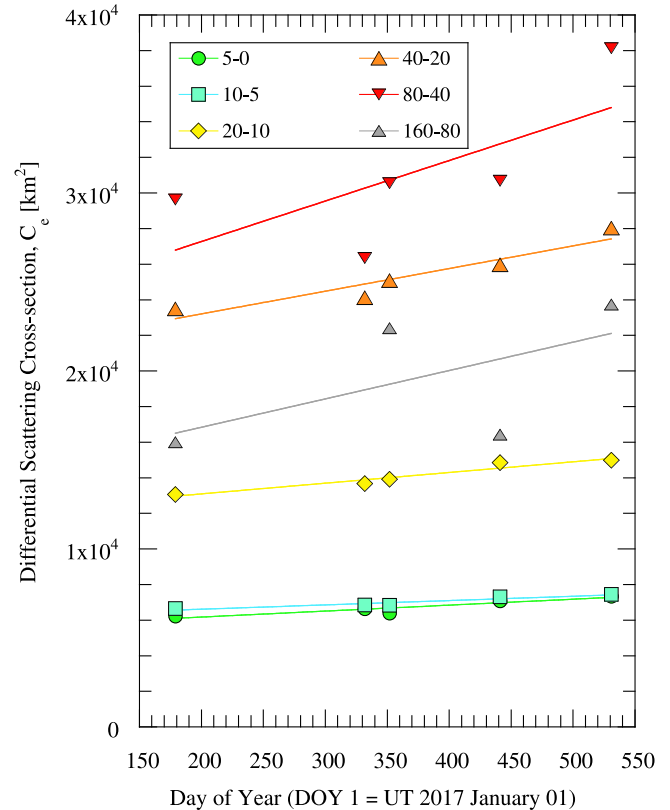


Figure 4. Differential scattering cross-section as a function of the date of observation for each of six photometry annuli. The radii of the apertures, expressed in units of 10^3 km, are indicated on the plot (e.g., 20–10 indicates the cross-section in the annulus with inner and outer radii of 10,000 and 20,000 km, respectively). Lines show least-squares fits to the data. The parameters of these fits are listed in Table 3.

~ 1 yr to reach the edge of the 160,000 km photometry aperture. We note that U is comparable to the gravitational escape speed from a nonrotating nucleus of density $\rho = 500 \text{kg m}^{-3}$ and radius $r_n = 9 \text{km}$ (the upper limit placed by Jewitt et al. 2017b), namely, $V_e = 4.8 \text{m s}^{-1}$. This coincidence suggests that the particles escaping into the coma are merely the fastest of a larger population of dust grains, many of which fell back onto the surface or into suborbital trajectories.

3.3. Dust Production Rates

The average dust mass production rate is given by

$$\frac{dM}{dt} = \frac{4}{3} \frac{\rho \bar{a} C_e}{\tau_r}, \quad (4)$$

Table 3
Fixed-aperture Photometry vs. Time

Radius ^a	f^b [km ²]	g^b [km ² day ⁻¹]	t_0 (days) ^c	τ_0 (yr) ^d	r_H (au) ^e
$C_e(5)-C_e(0)$	5515 ± 280	3.3 ± 0.7	-1671 ± 364	2012.4 ± 1.0	25.5 ± 1.6
$C_e(10)-C_e(5)$	6134 ± 184	2.4 ± 0.5	-2556 ± 538	2010.0 ± 1.5	29.3 ± 2.4
$C_e(20)-C_e(10)$	11896 ± 344	6.0 ± 0.9	-1982 ± 303	2011.6 ± 0.8	26.8 ± 1.2
$C_e(40)-C_e(20)$	20662 ± 984	12.7 ± 2.6	-1626 ± 342	2012.5 ± 0.9	25.2 ± 1.7
$C_e(80)-C_e(40)$	22727 ± 5279	22.7 ± 13.7	-1001 ± 647	2014.3 ± 1.8	22.0 ± 3.2
$C_e(160)-C_e(80)$	13651 ± 6003	15.9 ± 15.1	-859 ± 899	2014.6 ± 2.5	21.6 ± 4.3
Weighted Mean			-1772 ± 171	2012.1 ± 0.5	25.9 ± 0.9

Notes.

^a Projected radius of the photometry annulus, in units of 10³ km.

^b Coefficients f and g of the least-squares fit.

^c The initiation time, computed from $t_0 = f/g$, expressed as the number of days prior to UT 2017 January 01.

^d The initiation time, expressed in decimal year.

^e Heliocentric distance at time τ_0 , astronomical unit.

where ρ is the bulk density of the ejected solid material, \bar{a} is the weighted mean radius of the particles, C_e is the scattering cross-section in a photometric aperture and τ_r is the time of residence for dust in the aperture. To obtain a minimum estimate, we take $\bar{a} = 0.1$ mm, based on the simulations described in Section 3.2. The density of the particles depends on many unknowns, including their composition and their porosity; we assume $\rho = 500$ kg m⁻³. The cross-section inside the $\ell = 160,000$ km radius aperture is 119,000 km² (Table 2) and the residence time is $\tau_r = \ell/U$. We take $U = 4$ m s⁻¹ to find $\tau_r \sim 4 \times 10^7$ s. Then, Equation (4) gives an average mass-loss rate $dM/dt = 200$ kg s⁻¹ over the period 2012–2018. The corresponding mass in dust is $M \sim 10^{10}$ kg, also good to order of magnitude. Both M and dM/dt should be regarded as order-of-magnitude estimates, because they are based on several parameters (dust albedo, particle size, density, and ejection velocity) that are themselves individually uncertain.

We further represent the nucleus as a sphere of radius r_n and density ρ . The coma mass is then equal to the mass contained in a surface shell δr thick, where

$$\delta r = \frac{\tau_r}{4\pi\rho r_n^2} \frac{dM}{dt}. \quad (5)$$

Substituting for dM/dt from Equation (4) we obtain

$$\delta r = \frac{\bar{a}C_e}{3\pi r_n^2}. \quad (6)$$

All three variables in Equation (6) are observationally constrained. Again, taking minimum estimates, $C_e = 1.2 \times 10^5$ km² (Table 2), $\bar{a} \geq 0.1$ mm (Section 3.2), and $r_n \lesssim 9$ km (Jewitt et al. 2017b), gives $\delta r \gtrsim 1.5$ cm. The material in the coma at the time of observation is equal in mass to a surface shell around the nucleus of K2 only 1.5 cm thick. Of course, mass loss may be concentrated in a small fraction of the nucleus surface area, leading to much deeper local excavation, as we calculate in the next section.

3.4. Sublimation

Temperatures at K2 distances are so low that only substances more volatile than water ice could sublimate (Jewitt et al. 2017b; Meech et al. 2017). Carbon monoxide and carbon

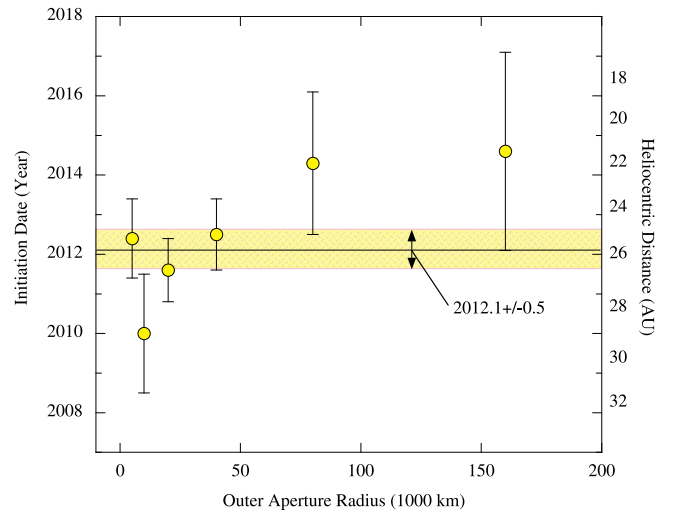


Figure 5. Plot of initiation date vs. the outer radius of the aperture used to estimate the date. The weighted mean initiation date is marked together with its $\pm 1\sigma$ uncertainty, shaded yellow. The right axis shows the heliocentric distance.

dioxide are two volatiles that are abundant in comets and capable of sublimating in the outer solar system. To calculate the rates of sublimation of these ices we use the equilibrium energy balance equation, neglecting conduction. In this approach, the ice is assumed to be exposed at the cometary surface and so the derived sublimation rates are upper limits to the true values to be expected if, as is likely, the ice is protected by even a thin, refractory layer. Given the lack of knowledge of the physical properties of K2, however, our simplistic approach provides useful intuition for understanding K2.

The energy balance equation is

$$\frac{L_\odot}{4\pi r_H^2} (1 - A_B) = \chi [\epsilon \sigma T^4 + L(T) f_s(T)]. \quad (7)$$

Here, L_\odot (W) is the luminosity of the Sun, r_H (m) is the heliocentric distance, A_B is the Bond albedo of the sublimating material, ϵ is the emissivity, $\sigma = 5.67 \times 10^{-8}$ (W m⁻² K⁻⁴) is the Stefan–Boltzmann constant, and $L(T)$ (J kg⁻¹) is the latent heat of sublimation of the relevant ice at temperature, T (K). The quantity f_s (kg m⁻² s⁻¹) is the sought-after mass flux of sublimated ice. The

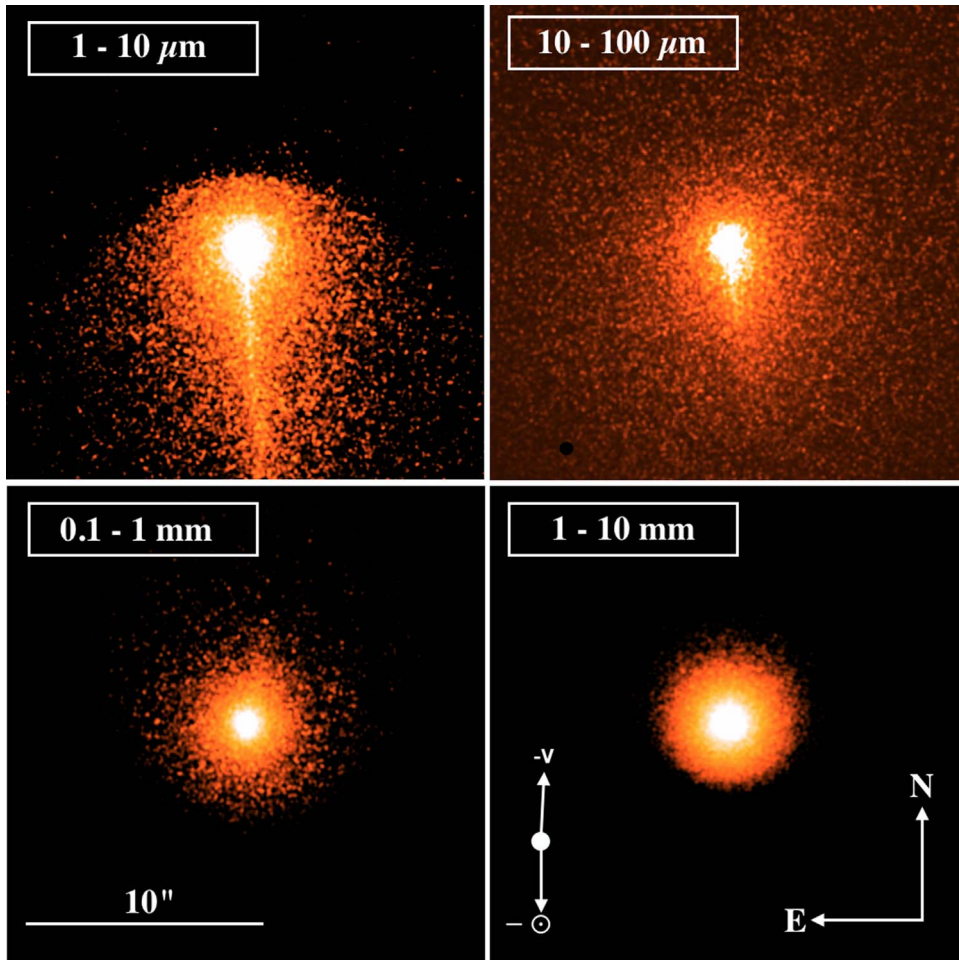


Figure 6. Monte Carlo models for UT 2018 June 15 in which only the sizes of the ejected particles are varied, as marked, to show the influence of radiation pressure. A scale bar, the cardinal directions and the projected anti-solar and negative velocity vectors are marked.

term on the left represents power absorbed from the Sun. The two terms on the right represent power radiated from the surface into space and power used to sublimate ice. Dimensionless parameter $1 \leq \chi \leq 4$ characterizes the way in which incident heat is distributed over the surface. To again focus on the highest possible sublimation rates for a given volatile, we consider sublimation from a flat surface oriented perpendicular to the Sun–comet line, for which $\chi = 1$, which approximates conditions found at the subsolar point on a nonrotating nucleus. To solve Equation (7) we assumed $L_{\odot} = 4 \times 10^{26}$ W, $\epsilon = 0.9$, and $A_B = 0.04$ and used ice thermodynamic parameters for CO and CO₂ from Brown & Ziegler (1980) and Washburn (1926).

The solutions to Equation (7) give $f_s \sim 2 \times 10^{-5} \text{ kg m}^{-2} \text{ s}^{-1}$ for CO and $f_s \sim 6 \times 10^{-6} \text{ kg m}^{-2} \text{ s}^{-1}$ for CO₂, both for $r_H = 16$ au, and these are peak values because we have assumed that the ice is located at the subsolar point on K2, this being the hottest spot. In order to supply a dust production rate, $dM/dt \sim 200 \text{ kg s}^{-1}$, would require a sublimating area

$$A_s = \frac{dM/dt}{f_{dg} f_s}, \quad (8)$$

where f_{dg} is the ratio of the dust to gas mass production rates. This quantity is unmeasured in distant comets, but in Jupiter family comets close to the Sun it is generally >1 (e.g., Reach et al. 2000; Fulle et al. 2016). We conservatively adopt $f_{dg} = 5$

and find, from Equation (8), sublimation areas $A_s = 2 \times 10^6 \text{ m}^2$ (2 km²) for CO and $A_s = 6 \times 10^6 \text{ m}^2$ (6 km²) for CO₂. Both values are small compared to the surface area of a 9 km radius nucleus ($4\pi r_n^2 \sim 10^3 \text{ km}^2$) showing that even a small patch of exposed ice can account for the observed activity. The surface erosion rate due to sublimation is $dr_n/dt = f_s/\rho$ (m s⁻¹). With density $\rho = 500 \text{ kg m}^{-3}$, we find $dr_n/dt \sim 1.2 \text{ m yr}^{-1}$ for CO and $\sim 0.4 \text{ m yr}^{-1}$ for CO₂. In the 6 years since activity began, sublimation would have eroded the nucleus locally by a very modest $\delta r \lesssim 10$ m, perhaps creating pit and cliff morphology like that observed on the nucleus of 67P/Churyumov–Gerasimenko.

3.5. The Cohesion Bottleneck

The escaping gas must have enough momentum to drag dust particles from the nucleus. A minimum condition is obtained by simply equating the gas drag force with the weight of the dust particle, as was done first by Whipple (1950). From this condition we calculate a_c , the radius of the largest grain that gas can eject against nucleus gravity, from

$$a_c(r_H) = \frac{9C_D V_g(r_H) f_s(r_H)}{16\pi G \rho \rho_n r_n}. \quad (9)$$

Quantity C_D is a dimensionless drag coefficient representing the efficiency with which gas momentum is transferred to the

grain, V_g is the gas outflow speed, ρ and ρ_n are the densities of the grains and nucleus, respectively, and r_n is the nucleus radius. We assume $C_D = 1$, $\rho_n = \rho = 500 \text{ kg m}^{-3}$, $V_g = 100 \text{ m s}^{-1}$, and $r_n = 9 \text{ km}$. The numerical constants in Equation (9) are specific to the assumption of spherical particles and should not be regarded as important. What matters is that a_c is most sensitive to f_s , evaluated from Equation (7).

Equation (9) is a necessary but not sufficient condition for grain ejection because of the existence of interparticle cohesive forces, as clearly described by Gundlach et al. (2015). Experiments show that the cohesive strength of micron-sized aggregates is about 150 N m^{-2} , and that the strength scales inversely with the size (Sánchez & Scheeres 2014). Accordingly, the cohesive strength of an assemblage of particles of radius a may be written as

$$S = S_0/a, \quad (10)$$

where $S_0 \sim 1.5 \times 10^{-4} \text{ (N m}^{-1}\text{)}$ and a is expressed in meters (see Sánchez & Scheeres 2014). Note that a slightly different size dependence ($S \propto a^{-2/3}$) is preferred by Gundlach et al. (2018). To estimate the effects of particle cohesion on the escape of particles, we compare the sublimation gas pressure, $P_s = f_s V_g$, where V_g is the thermal speed in the gas at the equilibrium sublimation temperature, T , with the cohesive strength, S . We set $P_s = S$ to find the critical radius, a_s , above which gas drag forces exceed the interparticle cohesion, finding

$$a_s(r_H) = \frac{S_0}{C_D f_s(r_H) V_g(r_H)}. \quad (11)$$

Again, we use Equation (7) to solve for f_s and V_g as functions of r_H and Equation (11) to calculate the critical radius, a_s . Note that $a_s \propto f_s^{-1}$, opposite to the dependence of a_c .

Equations (9) and (11) are plotted for CO sublimation in Figure 7 and for CO₂ sublimation in Figure 8. We refer to the point where the curves cross as the ‘‘cohesion bottleneck.’’ Setting $a_c = a_s$, we solve Equations (9) and (11) for

$$f_s = \left(\frac{16\pi G \rho \rho_n r_n S_0}{9C_D^2 V_g^2} \right)^{1/2} \quad (12)$$

and, by substitution, obtain $f_s = 10^{-4} \text{ kg m}^{-2} \text{ s}^{-1}$ at the bottleneck. By solution of Equation (7), this f_s is reached by CO at $r_H \sim 6.6 \text{ au}$ and CO₂ at $r_H \sim 4.5 \text{ au}$. At distances smaller than the crossing point, there exists a range of particles that are both small enough to be lifted against gravity and large enough to be lifted against cohesive forces. At distances larger than the crossing point, particles that are small enough to be lifted against nucleus gravity are trapped by interparticle cohesion. Our observations of millimeter-sized particles in distant comet K2 fall entirely in this latter regime, where interparticle cohesive forces prohibit grain ejection.

To emphasize that sublimation is unable to expel particles from the nucleus against interparticle cohesion, we plot solutions for the sublimation gas pressure from Equation (7) as a function of heliocentric distance in Figure 9. The figure shows a slightly higher sublimation pressure for CO (solid red curve) than for CO₂ (dashed blue curve), as expected from the greater volatility of CO. Also shown in Figure 9 are two estimates of the cohesive strength inferred for lunar regolith

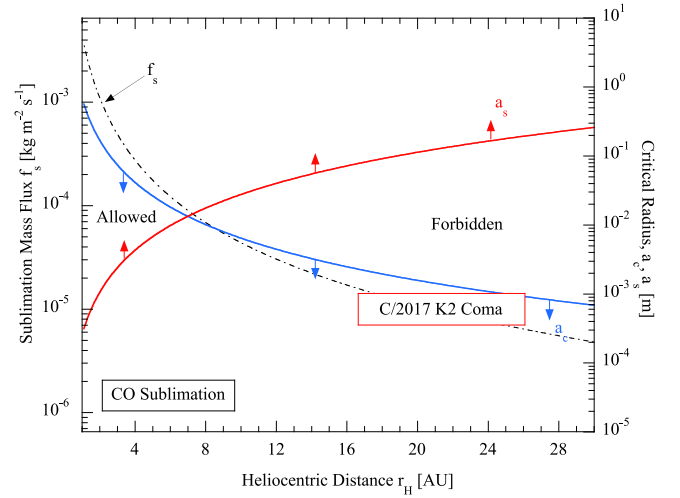


Figure 7. The equilibrium carbon monoxide specific sublimation rate (Equation (7)) is shown by the dashed black curve (left-hand axis). The blue curve shows the maximum ejectable dust grain radius against nucleus gravity as a function of heliocentric distance (Equation (9)). The red curve shows the minimum ejectable grain radius for overcoming interparticle cohesion (Equation (11)). To be ejected, a particle must plot above the red cohesion curve and below the blue gravity curve, which is impossible at the distance of K2. Critical radii are labeled on the right axis.

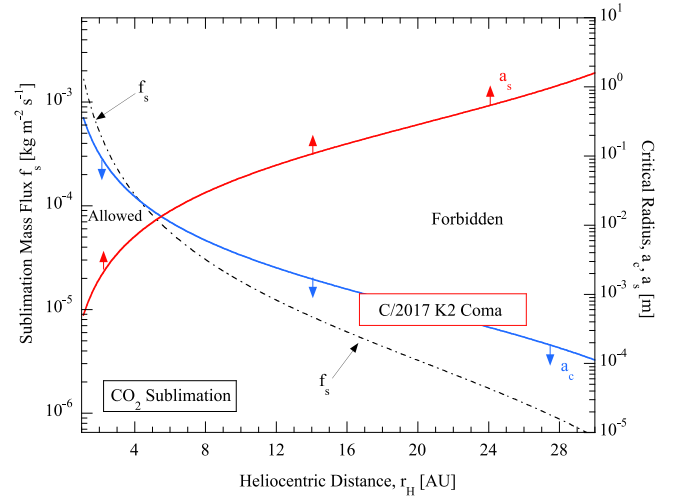


Figure 8. Same as Figure 7 but for carbon dioxide sublimation.

dust (Scott & Zuckerman 1971; Mitchell et al. 1972), for the fragmented active asteroid P/2013 R3 (Hirabayashi et al. 2014; Jewitt et al. 2014, 2017a) and for split comet P/Shoemaker–Levy 9 (Asphaug & Benz 1996), together with strength estimates from Equation (10) for three particle sizes. The sublimation gas pressures, even of CO, are 2–3 orders of magnitude too small to overcome the interparticle cohesion in the Sánchez & Scheeres (2014) model, and 4–6 orders of magnitude smaller than cohesive strengths measured in the regolith of the Moon, or inferred from break-up of P/2013 R3 and SL9.

We attempted to increase the calculated sublimation pressure by changing parameters in the sublimation Equation (7), without success. This is because, for volatile substances, the sublimation term already takes up a large fraction of the absorbed power, leaving little room for the radiation term to make a difference. The calculated pressures apply to free sublimation into a vacuum, matching the conditions at the

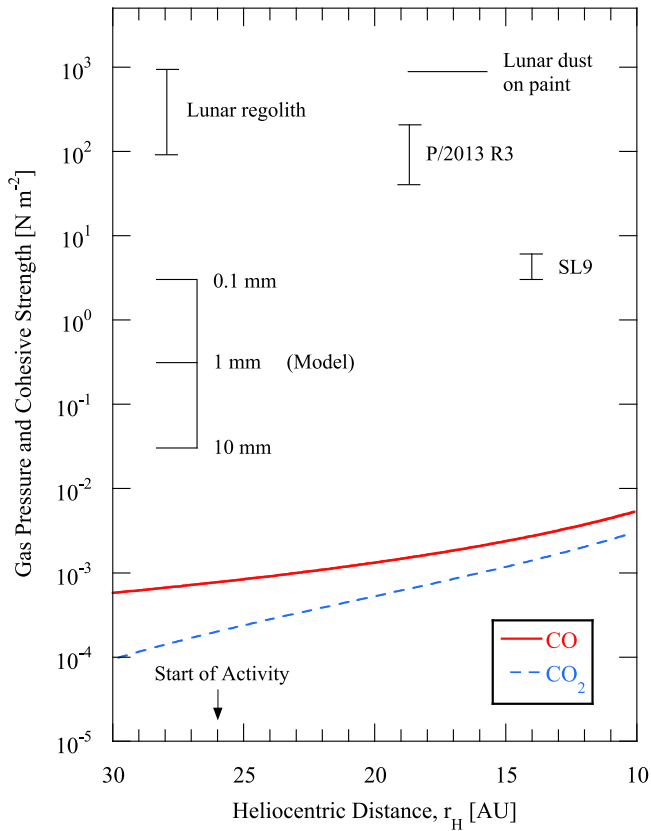


Figure 9. Gas pressure produced by the equilibrium sublimation of CO (solid red curve) and CO₂ (dashed blue curve) compared with cohesion estimates from several sources: Lunar regolith (Mitchell et al. 1972), Lunar dust adhering to paint (Scott & Zuckerman 1971), disrupted active asteroid P/2013 R3 (Hirabayashi et al. 2014; Jewitt et al. 2014, 2017a), tidally split P/Shoemaker-Levy 9 (SL9) (Asphaug & Benz 1996) and a cohesion model for three particle sizes (Sánchez & Scheeres 2014).

surface of a comet nucleus. Any increase in the temperature above the equilibrium value results in an increase in the sublimation rate (i.e., the energy is used to break intermolecular bonds in the ice), which quickly depresses the temperature back to the equilibrium value. Even setting $\epsilon = 0$ in Equation (7) (i.e., forcing all the absorbed energy into the sublimation term) increases the calculated $f_s(\text{CO})$ by only a few percent. The increase is larger (factor of 2.6) for $f_s(\text{CO}_2)$ but this still falls far short of the orders of magnitude strength gap in Figure 9. In this sense, the mechanism for the ejection of dust from K2 is a mystery. We expect that activity beyond the cohesion bottleneck is a general property of all distant comets.

3.6. Overcoming the Bottleneck

The failure of sublimation gas drag forces to overcome the cohesion bottleneck motivates brief consideration of other processes that might expel dust from comets at large heliocentric distances.

Prolonged exposure of cometary ices to the ionizing cosmic-ray flux is expected to cause molecular damage and the build-up of unstable radicals in a surface layer perhaps ~ 1 m thick (Cooper et al. 2003). Explosive recombination of these radicals upon warming by the Sun has been suggested as a source of activity in distant comets (Donn & Urey 1956) and could conceivably generate instantaneous gas pressure large enough to overcome the cohesion bottleneck. Unfortunately, the

steady-state coma surface brightness gradient (Figure 2) and the slow, monotonic brightening of K2 (Figure 4) are inconsistent with the burst-like activity that would result from recombination. Consequently, we do not consider explosive radical recombination to be plausible.

Impacts are occasionally suggested as causes of activity in distant comets (e.g., Cikota et al. 2018). However, even in the ecliptic the probability of impact is small and K2 (with inclination $i = 87^\circ.5$) is located far above the midplane of the solar system, leading to a negligible probability of collision. Furthermore, dust produced impulsively by an impact would violate the photometric and surface brightness evidence to the effect that the coma is long-lived (Figure 1), and produced in steady state (Figure 2). Neither would impacts selectively eject millimeter-sized debris, as observed. We confidently rule out the possibility of impact.

At ~ 25 au, even at the maximum possible (subsolar) temperature, $T_{SS} \sim 79$ K, the timescale for the crystallization of ice is comparable to the age of the solar system (Kouchi & Yamamoto 1995). Therefore, even if amorphous ice exists on K2, its crystallization can also be rejected as a mechanism for the observed early activity (see Jewitt et al. 2017b). Crystallization cannot become a significant source of gas until the comet has reached the $r_H \sim 10$ to 12 au region, if at all.

A related but different process known as “annealing” occurs when molecular bonds in amorphous ice locally rearrange, releasing trapped gases prior to larger-scale crystallization. We find only very limited experimental data about annealing in the literature (e.g., Ninio-Greenberg et al. 2017; Yokochi 2018), but these data suggest that it is unlikely to be a significant process in K2. For example, the experimentally determined fluxes of nitrogen exuded by annealing at 70 K are $\sim 10^{18}$ $\text{m}^{-2} \text{s}^{-1}$ (Ninio-Greenberg et al. 2017), corresponding to mass flux $f_s \sim 5 \times 10^{-8}$ $\text{kg m}^{-2} \text{s}^{-1}$. This is two to three orders of magnitude smaller than the CO sublimation mass flux at K2’s distance (Figure 7). We tentatively conclude that annealing offers no solution to overcoming the cohesion bottleneck.

Thermal fracture is another process that might operate at the very low temperatures present on K2, with the temperature contrast arising between the subsolar and night-side temperatures. This contrast is a function of both the thermal diffusivity and the rotation period, neither of which is known. Experiments show that ice at 77 K has a Young’s modulus, $Y = 1.8 \times 10^{10}$ N m^{-2} , and is very brittle, with fracture beginning at stresses $S \sim 3 \times 10^5$ N m^{-2} and failure (described by the authors as “explosive”) at $S \sim 4 \times 10^7$ N m^{-2} (Parameswaran & Jones 1975). Ignoring Poisson’s ratio, the strain induced by temperature difference δT is $\sigma \sim \epsilon \delta T$, where $\epsilon \sim 7 \times 10^{-6}$ K^{-1} is the expansivity at 77 K. Setting $Y = S/\sigma$, we solve to find

$$\delta T = \frac{S}{\epsilon Y} \quad (13)$$

and, by substitution we find $\delta T = 3$ K for first fracture and 300 K for failure. Of course, $\delta T = 300$ K can never be reached on a comet because the ice would sublimate away. Furthermore, the mechanical properties sampled in the laboratory are those of crystalline ice and amorphous ice in comets might have different values. Still, $\delta T = 3$ K is a very small temperature threshold for the onset of fracture and it is plausible that, upon approaching the Sun, diurnal temperature fluctuations could reach the level needed to fracture ice. Fracture is attractive because stored energy from thermal

stresses would be able to break the cohesion bottleneck, leaving particles free to be expelled against nucleus gravity alone.

Dielectric surfaces exposed to sunlight develop a positive charge as a result of the loss of photoelectrons. Evidence that particles can be levitated by near-surface electric fields comes from “horizon glow” observations on the Moon (Criswell & de 1977) and, with less certainty, from ponded particulates that have migrated across the surfaces of asteroids into local gravitational potential minima (Robinson et al. 2001). Unfortunately, the mechanism by which particles might be electrostatically detached from the lunar regolith is not understood, although it is highly relevant to understanding the cohesion bottleneck, in general, and the case of K2, in particular. The surface potential raised by photoionization is only ~ 5 V and, across a meter-thick Debye layer, the resulting electric field is only ~ 5 V m⁻¹. The resulting repulsive force is negligible compared to the weight and to cohesive forces.

Theoretical consideration of microscale supercharging suggests that, depending on the conductivity and other properties, huge electric fields (e.g., 10^5 V m⁻¹) might be generated between near-surface particles in a regolith (Zimmerman et al. 2016). In recent experiments this supercharging has been shown to launch $5 \mu\text{m}$ sized grains at ~ 1 m s⁻¹, almost sufficient to explain the lunar horizon glow (Wang et al. 2016). On a kilometer scale cometary nucleus, these launch velocities approach the gravitational escape speed and direct escape to the coma would be possible, even without the aid of post-detachment gas drag.

While promising, it is not obvious that an effect capable of detaching grains at the surface of the Moon can operate at the edge of the planetary region. For example, the ionizing flux varies as r_H^{-2} , meaning that the charging currents at 26 au will be ~ 700 times smaller than at 1 au, and the charging timescales 700 times longer. Charging times of 1 day at 1 au correspond to ~ 2 yr at 26 au. Long charging times will elevate the importance of leakage currents between nearby grains owing to finite electrical conductivity, thus making large potential differences and strong electric fields harder to attain. Moreover, the effect described in Wang et al. is still too weak to launch millimeter-sized grains at 4 m s⁻¹ and so it does not directly account for the coma of K2. Nevertheless, we remain cautiously optimistic that electrostatic supercharging can break the cohesion bottleneck and we encourage more work on this process.

Thermal fracture and electrostatic supercharging operate independently of gas drag and it must be considered possible that the coma of K2 is produced without the aid of gas. More likely, gas drag, fracture, and/or electrostatic supercharging operate in tandem to cause cometary activity at ultra-large heliocentric distances. As K2 approaches the Sun, the role of nonthermal effects will diminish relative to the rising sublimation mass flux, culminating in the entry of the comet into the “allowed” region of Figures 7 and 8.

3.7. The Future

The slow approach of K2 toward perihelion on 2022 December 21, at $r_H = 1.810$ au, offers the opportunity to examine previously unstudied changes in an inbound Oort cloud comet. We anticipate a change in the style of mass loss with the onset of crystallization at about $r_H \lesssim 12$ au (starting early 2019) and another change as the comet approaches the orbit of Jupiter (5 au, in late 2021), where water ice can begin to sublimate. Water ice grains in the coma will

themselves sublimate at this distance, leading to a decrease in the scattering cross-section even as nucleus activity rises. Thus, it is impossible to predict the brightness evolution of the comet, with brightening caused by increased heating of the nucleus by the Sun, perhaps augmented by exothermic crystallization and the release of trapped gas, but countered by a fading due to the loss of ice from dust grains in the coma.

4. Summary

New measurements of inbound, long-period comet C/2017 K2 at heliocentric distances $r_H = 15.9$ to 13.8 au, give the following main results:

1. Extrapolation of the photometry shows that mass loss from K2 started in 2012.1 ± 0.5 (when $r_H = 25.9 \pm 0.9$ au).
2. Dust is released continuously and in steady state, as shown by the surface brightness gradient of the coma, $m = -1.010 \pm 0.004$. The gradient is inconsistent with a coma produced by impulsive activity such as that which might result from an outburst, allowing us to rule out gas release from the explosive recombination of radicals, and interplanetary impacts, as plausible sources of distant activity in C/2017 K2. The comet is also far too cold for crystallization of amorphous ice to drive the coma.
3. We find that the optically dominant particles are large (radius $\gtrsim 0.1$ mm), rendering them insensitive to deflection by solar radiation pressure and explaining why the isophotes of the coma are persistently circular. Dust ejection speeds, ~ 4 m s⁻¹, are small compared to the thermal speed in gas ($\sim 10^2$ m s⁻¹) but comparable to the ~ 5 m s⁻¹ gravitational escape speed of a few kilometer radius nucleus. The order-of-magnitude dust mass-loss rate is ~ 200 kg s⁻¹.
4. Drag forces from sublimating supervolatiles (e.g., CO, but to a lesser extent, CO₂) exceed the gravitational attraction to the nucleus for millimeter-sized and smaller particles. However, these drag forces are orders of magnitude too small to overcome interparticle cohesion, defining the “cohesion bottleneck” and raising the puzzle of how dust ejection at large distances is possible.
5. We suggest thermal fracture and electrostatic supercharging in the cometary regolith (the latter recently postulated to explain horizon glow observations on the Moon) as two previously neglected processes having the potential to overcome the cohesion bottleneck.

We thank Bin Yang and Quanzhi Ye for reading the paper. Based on observations made under GO 15409 and 15423 with the NASA/ESA *Hubble Space Telescope*, obtained at the Space Telescope Science Institute, operated by the Association of Universities for Research in Astronomy, Inc., under NASA contract NAS 5-26555. J.A. appreciates funding from European Research Council Starting grant No. 757390.

Facility: *HST*.

ORCID iDs

Jessica Agarwal  <https://orcid.org/0000-0001-6608-1489>
 Man-To Hui  <https://orcid.org/0000-0001-9067-7477>
 Jing Li  <https://orcid.org/0000-0002-0982-7309>
 Max Mutchler  <https://orcid.org/0000-0002-0088-3021>
 Harold Weaver  <https://orcid.org/0000-0003-0951-7762>

References

- Asphaug, E., & Benz, W. 1996, *Icar*, **121**, 225
- Brown, G., & Ziegler, W. 1980, *Adv. Cryog. Eng.*, 25, 662
- Cikota, S., Fernández-Valenzuela, E., Ortiz, J. L., et al. 2018, *MNRAS*, **475**, 2512
- Cooper, J. F., Christian, E. R., Richardson, J. D., & Wang, C. 2003, *EM&P*, **92**, 261
- Criswell, D. R., & de, B. R. 1977, *JGR*, **82**, 999
- Donn, B., & Urey, H. C. 1956, *ApJ*, **123**, 339
- Fulle, M., Altobelli, N., Buratti, B., et al. 2016, *MNRAS*, **462**, S2
- Gundlach, B., Blum, J., Keller, H. U., & Skorov, Y. V. 2015, *A&A*, **583**, A12
- Gundlach, B., Schmidt, K. P., Kreuzig, C., et al. 2018, *MNRAS*, **479**, 1273
- Hirabayashi, M., Scheeres, D. J., Sánchez, D. P., & Gabriel, T. 2014, *ApJL*, **789**, L12
- Hui, M.-T., Jewitt, D., & Clark, D. 2018, *AJ*, **155**, 25
- Jewitt, D., Agarwal, J., Li, J., et al. 2014, *ApJL*, **784**, L8
- Jewitt, D., Agarwal, J., Li, J., et al. 2017a, *AJ*, **153**, 223
- Jewitt, D., Hui, M.-T., Mutchler, M., et al. 2017b, *ApJL*, **847**, L19
- Jewitt, D. C., & Meech, K. J. 1987, *ApJ*, **317**, 992
- Kouchi, A., & Yamamoto, T. 1995, *Prog. Crystal Growth and Charact.*, 30, 83
- Królikowska, M., & Dybczyński, P. A. 2018, *A&A*, **615**, A170
- Meech, K. J., Kleyna, J. T., Hainaut, O., et al. 2017, *ApJL*, **849**, L8
- Mitchell, J. K., Scott, R. F., Houston, W. N., et al. 1972, *LPSC*, **3**, 545
- Ninio-Greenberg, A., Laufer, D., & Bar-Nun, A. 2017, *MNRAS*, **469**, S517
- Parameswaran, V., & Jones, S. 1975, *JGlac*, **14**, 305
- Reach, W. T., Sykes, M. V., Lien, D., & Davies, J. K. 2000, *Icar*, **148**, 80
- Robinson, M. S., Thomas, P. C., Veverka, J., Murchie, S., & Carcich, B. 2001, *Natur*, **413**, 396
- Sánchez, P., & Scheeres, D. J. 2014, *M&PS*, **49**, 788
- Scott, R. F., & Zuckerman, K. A. 1971, *LPSC*, **2**, 2743
- Sekanina, Z. 1973, *ApL*, **14**, 175
- Sekanina, Z. 1975, *Icar*, **25**, 218
- Sekanina, Z. 1982, *AJ*, **87**, 161
- Wang, X., Schwan, J., Hsu, H.-W., Grün, E., & Horányi, M. 2016, *GeoRL*, **43**, 6103
- Washburn, E. 1926, *International Critical Tables of Numerical Data, Physics, Chemistry and Technology*, Vol. 3 (New York: McGraw-Hill)
- Whipple, F. L. 1950, *ApJ*, **111**, 375
- Ye, Q.-Z., & Hui, M.-T. 2014, *ApJ*, **787**, 115
- Yokochi, R. 2018, *LPSC*, **49**, 2957
- Zimmerman, M. I., Farrell, W. M., Hartzell, C. M., et al. 2016, *JGRE*, **121**, 2150